

1  
2  
3  
4  
5  
6  
7  
8  
9  
10 **High precision registration between zebrafish brain atlases**  
11 **using symmetric diffeomorphic normalization**  
12  
13  
14  
15  
16  
17  
18  
19  
20  
21

22 Gregory D. Marquart<sup>1,2</sup>, Kathryn M. Tabor<sup>1</sup>, Eric J. Horstick<sup>1</sup>, Mary Brown<sup>1</sup>,  
23 Alexandra K. Geoca<sup>1</sup>, Nicholas F. Polys<sup>3</sup>, Damian Dalle Nogare<sup>1</sup> and Harold A. Burgess<sup>1\*</sup>  
24  
25  
26  
27  
28  
29  
30  
31  
32  
33  
34  
35  
36

37 <sup>1</sup> Division of Developmental Biology, *Eunice Kennedy Shriver* National Institute of Child Health  
38 and Human Development, Bethesda, MD 20892

39 <sup>2</sup> Neuroscience and Cognitive Science Program, University of Maryland, College Park, MD  
40 20742

41 <sup>3</sup> Advanced Research Computing, Department of Computer Science, Virginia Polytechnic  
42 Institute and State University, Blacksburg, VA 24061

43  
44  
45  
46  
47  
48  
49 \* Contact: burgessha@mail.nih.gov ; 301-402-6018  
50  
51  
52  
53

54 Running title: High fidelity inter-atlas registration using ANTs SyN transform

55 Keywords: zebrafish, atlas, ANTs, SyN, registration, diffeomorphism, normalization, brain  
56 imaging, transgenic, virtual reality, Unity, X3D  
57  
58  
59  
60  
61

## Abstract

Atlases provide a framework for information from diverse sources to be spatially mapped and integrated into a common reference space. In particular, brain atlases allow regional annotation of gene expression, cell morphology, connectivity and activity. In larval zebrafish, advances in genetics, imaging and computational methods have enabled the collection of large datasets providing such information on a whole-brain scale. However, datasets from different sources may not be aligned to the same spatial coordinate system, because technical considerations may necessitate use of different reference templates. Two recent brain atlases for larval zebrafish exemplify this problem. The Z-Brain atlas contains information on gene expression, neural activity and neuroanatomical segmentation acquired using immunohistochemical staining of fixed tissue. In contrast, the Zebrafish Brain Browser (ZBB) atlas was constructed from live scans of fluorescent reporter genes in transgenic larvae. Although different reference brains were used, the two atlases included several transgene patterns in common that provide potential 'bridges' for transforming each into the other's coordinate space. We tested multiple bridging channels and registration algorithms. The symmetric diffeomorphic normalization (SyN) algorithm in ANTs improved the precision of live brain registration while better preserving cell morphology than the previously used B-spline elastic registration algorithm. SyN could also be calibrated to correct for tissue distortion introduced during fixation and permeabilization. Multi-reference channel optimization provided a transformation that enabled Z-Brain and ZBB to be co-aligned with high precision and minimal perturbation of cell and tissue morphology. Finally, we developed software to visualize brain regions in 3-dimensions, including a virtual reality neuroanatomy explorer. This study demonstrates the feasibility of integrating whole brain datasets, despite disparate reference templates and acquisition protocols, when sufficient information is present for bridging. This increased accuracy and interoperability of digital brain atlases in larval zebrafish will facilitate future neurobiological studies.

## Background

Larval stage zebrafish are an increasingly popular model for neurobiological studies. With a brain that contains an estimated  $10^5$  neurons, larvae are similar in complexity to adult *Drosophila*, another established neuroscience model. In both systems, researchers can deploy a wide range of genetic tools in efforts to decode patterns of neural structure and connectivity. In larval zebrafish, optical transparency and constrained physical dimensions (fitting within an imaging volume of  $1000 \times 600 \times 350 \mu\text{m}$ ) allow the entire brain to be rapidly scanned at cellular resolution using diffraction-limited microscopy. In principle, this enables researchers to systematically analyze effects of manipulations on a brain-wide level. However, such efforts have been hampered by the absence of a comprehensive digital atlas that

1  
2  
3  
4 36 would provide researchers with a unified framework in which to aggregate data from different  
5  
6 37 experiments and gain deeper insights from correlations between neuronal cell identity, connectivity, gene  
7  
8 38 expression and function within the brain. Additionally, digital atlases may more clearly delineate  
9  
10 39 structural boundaries that are difficult to accurately identify within individual brains, allowing for a more  
11 40 rigorous mapping of neuroanatomical regions onto experimental data.  
12  
13 41

14 42 These longstanding problems in zebrafish neuroscience have recently been addressed by the construction  
15  
16 43 of digital atlases using three-dimensional (3D) image registration techniques: the Virtual Brain Explorer  
17  
18 44 for Zebrafish (ViBE-Z), Z-Brain and the Zebrafish Brain Browser (ZBB) [1–3]. In these atlases,  
19  
20 45 information on gene expression, structure (neuronal cell bodies, glia, vasculature, ventricles, neuropil or  
21  
22 46 axon tracts) and measures of activity (calcium or secondary messenger activity) are consolidated within a  
23  
24 47 common spatial framework. By using widely-available transgenic lines or immunohistochemical stains as  
25  
26 48 reference templates for brain alignment, each of these atlases provides other researchers the opportunity  
27  
28 49 to register their own datasets into these digital spaces and take advantage of the information contained  
29  
30 50 within.  
31  
32 51

33 52 ViBE-Z was the first comprehensive three-dimensional digital brain atlas in zebrafish that used a nuclear  
34  
35 53 stain for the alignment of 85 high resolution scans comprising 17 immunohistochemical patterns at 2–4  
36  
37 54 days post-fertilization (dpf) [3,4]. In ViBE-Z, custom algorithms were developed to correct for variations  
38  
39 55 in fluorescent intensity with scan depth, and a landmark approach taken to perform accurate image  
40  
41 56 registration and segmentation into 73 neuroanatomic regions.  
42  
43 57

44 58 In contrast, two more recent approaches (Z-Brain and ZBB) have generated brain atlases at 6 dpf through  
45  
46 59 non-linear B-spline registration using the freely available Computational Morphometry Toolkit (CMTK)  
47  
48 60 [5,6]. Z-Brain includes 29 immunohistochemical patterns from 899 scans which form the basis for expert  
49  
50 61 manual segmentation of the brain into 294 neuroanatomic regions. These partitions facilitate the analysis  
51  
52 62 of phospho-ERK expression for mapping neural activity [2]. In Z-Brain, each expression pattern was co-  
53  
54 63 scanned with tERK immunoreactivity, and registered to a single tERK-stained reference brain. For ZBB,  
55  
56 64 we live-imaged 354 brains from 109 transgenic lines and manually annotated the expression found in  
57  
58 65 each [1]. In place of tERK, a single *vglut2a:dsRed* transgenic brain was used as the reference in ZBB with  
59  
60 66 transgenic lines crossed and co-imaged with this channel for registration. Brain browser software enables  
61  
62 67 researchers to select a transgenic line labeling a selected set of neurons for monitoring and manipulating  
63  
64 68 circuit function.  
65  
66 69

1  
2  
3  
4 70 While Z-Brain and ZBB are powerful datasets on their own, we saw an opportunity to merge the two  
5  
6 71 atlases because they are both based on confocal scans of 6 dpf larvae. This would bring to Z-Brain a large  
7  
8 72 number of additional transgenic lines and to ZBB, the expert manual segmentation of Z-Brain. Several  
9  
10 73 similarities between Z-Brain and ZBB suggested that bridging the atlases would be possible. First as  
11  
12 74 zebrafish rearing conditions are standardized across laboratories and fish were imaged at the same time  
13  
14 75 post-fertilization, Z-Brain and ZBB likely reflect the same developmental timepoint. Second, images in  
15  
16 76 both atlases were acquired at similar resolution (0.8 x 0.8 x 2  $\mu\text{m}$  for Z-Brain; 1 x 1 x 1 or 1 x 1 x 2  $\mu\text{m}$   
17  
18 77 for ZBB) and orientation (dorsal to ventral horizontal scans). Third, despite using distinct templates  
19  
20 78 (tERK for Z-Brain and *vglut2a* for ZBB), Z-Brain and ZBB have several transgenic markers in common,  
21  
22 79 which provided the possibility of bridging the datasets by using these shared patterns as references for a  
23  
24 80 secondary registration step.

25  
26 81  
27  
28 82 One of the strengths of larval zebrafish is the ability to rapidly image at cellular resolution and visualize  
29  
30 83 brain-wide neuronal morphology, providing valuable information on cell type and potential connectivity.  
31  
32 84 Z-Brain and ZBB both illustrate the feasibility of performing whole-brain registration with precision  
33  
34 85 sufficient to ensure that the 'same' neurons from different fish are aligned to within a cell diameter (~10  
35  
36 86  $\mu\text{m}$ ). However, a challenge for brain registration in zebrafish is to minimize local distortions, so that  
37  
38 87 cellular morphology is preserved while still allowing sufficient deformation to overcome biological  
39  
40 88 variability between individual brains or malformations due to tissue processing.

41  
42 89  
43  
44 90 Here we describe a method to co-register ZBB and Z-Brain, bridging the two existing 6 dpf larval  
45  
46 91 zebrafish brain atlases. By using the diffeomorphic algorithm SyN in the Advanced Normalization Tools  
47  
48 92 (ANTs) software package [7,8], we were able to overcome differences in tissue shape due to fixation,  
49  
50 93 optimize the trade-off between preservation of cell morphology and global alignment, and provide precise  
51  
52 94 registration in all tested brain regions. Additionally, ANTs provided superior image registration for live-  
53  
54 95 scanned larvae, enabling us to improve the precision of registration and neuron morphology within our  
55  
56 96 original ZBB atlas, allowing us to compile a new version with increased fidelity (ZBB<sub>1.2</sub>).

57  
58 97

## 59 98 **Methods**

60  
61 99

### 62 100 **Zebrafish lines.**

63 101 In order to provide additional options for bridging ZBB and Z-Brain, we scanned two transgenic lines that  
64  
65 102 were not in the original ZBB release: *Et(gata2a:EGFP)zf81 (vmat2:GFP)* and *Tg(isll:GFP)rw0*  
66  
67 103 (*isll:GFP*) [9,10]. Aside from the use of ANTs, the basic imaging and registration workflow was

1  
2  
3  
4 104 performed as previously described [1]. Other lines referenced in this study are *Tg(slc6a3:EGFP)ot80*  
5  
6 105 (*DAT:GFP*) [11], *Tg(-3.2fev:EGFP)ne0214 (Pet1:GFP)* [12], *y264Et* [13], *s1181tEt* [14],  
7  
8 106 *Tg(gad1b:GFP)nns25 (gad1b:GFP)* [15], *Tg(slc6a5:GFP)cf3 (glyT2:GFP)* [16], *Tg(-17.6isl2b:GFP)zc7*  
9  
10 107 (*isl2b:GFP*) [17], *Tg(-3.4tph2:Gal4ff)y228 (tph2:Gal4)* [18], *TgBAC(slc17a6b:lox-DsRed-lox-*  
11  
12 108 *GFP)nns14 (vglut2a:dsRed)* [19], *Tg(slc17a6:EGFP)zf139* [20],  
13  
14 109 *Tg(elavl3:CaMPARI(W391F+V3987L))jf9* [21], *Tg(phox2b:GFP)w37* [22], *J1229aGt* [23] and several  
15  
16 110 Gal4 enhancer traps from ZBB: *y304Et*, *y332Et*, *y341Et*, *y351Et* and *y393Et* [1]. All *in vivo* experimental  
17  
18 111 protocols were approved by the NICHD animal care and use committee.  
19

### 20 113 **Immunohistochemistry.**

21 114 Immunolabeling was as described [2] with the following adaptations. Larvae were fixed overnight at 4°C  
22  
23 115 in PBS with 4% paraformaldehyde and 0.25% Triton X-100. Samples were then washed in PBS  
24  
25 116 containing 0.1% Triton X-100 (PBT) 3 times for 5 min. For antigen retrieval, samples were incubated in  
26  
27 117 150 mM Tris-HCl pH 9.0 for 5 min, followed by 15 min at 70°C and washed in PBT 2 times for 5 min  
28  
29 118 [24]. Critically, samples were then permeabilized on ice in fresh 0.05% trypsin-EDTA for no more than 5  
30  
31 119 minutes. If pigmented, samples were incubated in PBT with 1.5% H<sub>2</sub>O<sub>2</sub> and 50 mM KOH for 15 min,  
32  
33 120 rinsed 2 times in PBT and washed again for 10 min. Samples were then blocked in PBT containing 5%  
34  
35 121 normal goat serum (NGS) and 0.2% bovine serum albumin (BSA) for 1 hr before incubation at 4°C with  
36  
37 122 tERK antibodies (Cell Signaling, 4696) diluted 1:500 in PBT with 5% NGS and 0.2% BSA for a  
38  
39 123 minimum of 6 hr. Samples were then washed with PBT 4 times for 30 min before incubation at 4°C for a  
40  
41 124 minimum of 2 hr with fluorescent secondary antibodies (Alexa Fluor 488 or 548) diluted 1:1000 in PBT  
42  
43 125 with 5% NGS and 0.2% BSA. Samples were finally rinsed 4 times for 30 min prior to imaging.  
44

### 45 127 **Registration.**

46 128 Registrations were performed using CMTK version 3.2.3 and ANTs version 2.1.0 running on the National  
47  
48 129 Institute of Health's Biowulf Linux computing cluster. Registrations were parallelized using Slurm-based  
49  
50 130 bash scripts available upon request. For CMTK, previously optimized registration parameters that  
51  
52 131 minimize computation time while maximizing precision were used (`registrationx --dofs 12 --min-stepsize`  
53  
54 132 `1 and warpx --fast --grid-spacing 100 --smoothness-constraint-weight 1e-1 --grid-refine 2 --min-stepsize`  
55  
56 133 `0.25 --adaptive-fix-thresh 0.25`). For ANTs registrations, the parameters used are cited in the relevant text  
57  
58 134 and figures with optimized parameters listed in Table 1. Image volumes were rendered within the  
59  
60 135 Zebrafish Brain Browser (ZBB), ImageJ [25] or code written in IDL (Harris Geospatial Solutions). For  
61  
62 136 the conversion to/from Nifti format required for ANTs, we used the ImageJ plugin `nifti_io.jar` written by  
63  
64 137 Guy Williams [26].  
65

1  
2  
3  
4  
5  
6  
7  
8  
9  
10  
11  
12  
13  
14  
15  
16  
17  
18  
19  
20  
21  
22  
23  
24  
25  
26  
27  
28  
29  
30  
31  
32  
33  
34  
35  
36  
37  
38  
39  
40  
41  
42  
43  
44  
45  
46  
47  
48  
49  
50  
51  
52  
53  
54  
55  
56  
57  
58  
59  
60  
61  
62  
63  
64  
65

138

**Volume rendering & 3D visualization.**

140

141 Binary masks corresponding to 25 anatomical regions from Z-Brain aligned to ZBB were converted into  
142 meshes using the Create Surfaces tool in the IntSeg\_3D.jar plugin for ImageJ [27]. Edges for individual  
143 meshes were iteratively reduced below 5000 and vertices (single-precision floating-points of the  
144 triangular meshes) written as OBJ files. As there is no intrinsic color or color conventions as of yet for  
145 these brain structures, we used color hue as a nominal categorical coding for each region. To maximize  
146 accessibility, we rendered meshes in Extensible 3D (X3D) format, an ISO (International Organization for  
147 Standardization) standard developed by the not-for-profit Web3D Consortium [28]. This format allows  
148 portability between numerous tools and applications as well as deployment across a broad spectrum of  
149 platforms. For the rendering, previously generated OBJs were transcoded into ImageTextureAtlas PNGs  
150 used X3D's standard IndexedFaceSet to represent mesh information and then tiled at different resolutions  
151 (4096 & 8192 pixels squared) using AtlasConversionScripts [29]. Additionally, dask and pyimg python  
152 libraries were used to generate volume norms (image and ImageTextureAtlas files) by gradient descent.  
153 All renderings were then merged into a single X3D XML scene which was losslessly compressed (in  
154 SRC/glTF) to a final size of 4.5 MB. This makes the scene compact enough to be visualized on a cell  
155 phone, yet still retaining details for visualization and editing in more immersive virtual reality  
156 environments. Finally, X3D files were published to HTML5 via the X3DOM library and a simple user  
157 interface created that allows for the visibility of different structures to be toggled on and off. Brain  
158 meshes were converted to FBX files for import into Unity using Blender 2.78a (Blender foundation,  
159 Amsterdam, NL) and mobile app development for Google Cardboard VR headsets performed in Unity  
160 5.4.2 (Unity Technologies SF, San Francisco CA) using the Google VR for Unity SDK (Google,  
161 Mountain View CA). Custom scripts controlling movement and mesh display were written for Unity in  
162 C#.

163

**Statistics.**

165

166 Cross correlation between registered image sets was performed using the c\_correlate function within IDL  
167 version 7.0. Correlations were run within small sub-regions of the registered image volumes. In Fig. 1,3  
168 & 4, 50  $\mu\text{m}$  side cube sub-regions were manually defined by selecting volumes containing high contrast  
169 boundaries. For cross correlations between individual brains scanned for each transgenic line in ZBB (Fig  
170 2a,b), 40  $\mu\text{m}$  side cubes were drawn around the three computationally identified brightest sub-regions  
171 within the expression pattern, with cross-correlation then calculated between all pairs of brains. The mean  
of all cross-correlations was used to estimate registration precision.

1  
2  
3  
4  
5  
6  
7  
8  
9  
10  
11  
12  
13  
14  
15  
16  
17  
18  
19  
20  
21  
22  
23  
24  
25  
26  
27  
28  
29  
30  
31  
32  
33  
34  
35  
36  
37  
38  
39  
40  
41  
42  
43  
44  
45  
46  
47  
48  
49  
50  
51  
52  
53  
54  
55  
56  
57  
58  
59  
60  
61  
62  
63  
64  
65

172

**Results**

174

**Optimization of ANTs based registration of live *vglut2a:dsRed* image scans**

176

Brain registration in Z-Brain and ZBB used the B-spline elastic transformation in CMTK. Before attempting to co-align Z-Brain and ZBB, we tested an alternate algorithm for brain alignment, the diffeomorphic symmetric normalization (SyN) method in ANTs, because: (1) SyN has been shown to outperform B-spline transformations for deformable image registration in a variety of imaging modalities [30,31]. (2) ANTs permits registration using multiple reference channels, potentially allowing the use of multiple complementary expression patterns as references for improved registration fidelity. (3) By calculating forward and reverse transformations simultaneously, SyN transformation matrices are intrinsically symmetric, ensuring that bridging registrations would be unbiased and that we could easily perform reciprocal transformations to register each dataset into the other's coordinate system.

186

We first calibrated registration conditions by assessing alignment precision for a representative *vglut2a:DsRed* scan registered to the original *vglut2a:DsRed* reference brain in ZBB (*vglut2a<sub>ZBB</sub>*; file *vglut-dsred-ref-01.nii.gz*, available from [32]). Similar to CMTK we employed a three step registration within ANTs where rigid and affine steps were used to initialize a deformable registration using the SyN diffeomorphic transformation with cross correlation (CC) as the similarity metric. We tested a range of values for each of the SyN parameters as well as the radius of the region used for cross correlation.

193

While we previously used brain-wide normalized cross correlation (NCC) to evaluate registration [1], correlation within local anatomical regions that contain discrete landmarks has been shown to be a more reliable criterion for quantitatively assessing registration precision [33]. Accordingly, in this work we quantified precision in two ways; by measuring local registration errors both computationally as well as manually. For the computational measure, we identified a set of 12 landmarks within the *vglut2a* pattern, each within a 50  $\mu$ m side cube. Landmarks were broadly distributed in the hope of representing diverse brain regions and minimizing the bias for any single structure. We measured the cross-correlation between the corresponding regions in *vglut2a<sub>ZBB</sub>* and the registered image, then calculated the mean of the cross correlation between all regions (MCC ; Fig. 1a). For the manual measure of precision, we identified 10 landmarks in the *vglut2a<sub>ZBB</sub>* pattern that could be visually recognized (landmark positions are described in Additional File 1), and calculated the mean landmark distance (MLD) from the corresponding points in the registered image as assessed by three blinded experts. We also assessed the

1  
2  
3  
4 206 results visually to subjectively assess the severity of tissue distortion. Unsurprisingly, similar to our  
5  
6 207 previous work with brain-wide NCC, images with the highest MCCs generally showed more conspicuous  
7  
8 208 tissue distortion — thus although greater precision was achieved with increased deformation, we  
9  
10 209 preferred results where cell shape and axon tract morphology were preserved (Fig. 1b,c). Disregarding  
11  
12 210 parameter combinations that resulted in overt distortion, we identified a set of values (Table 1, **live**  
13  
14 211 **registration**) where cell morphology remained intact, but registration precision (MCC) was maximized.  
15  
16 212 With these parameters, although the MCC for *vglut2a* improved only slightly from 0.79 using CMTK to  
17  
18 213 0.81 using SyN, cell morphology was noticeably better preserved, especially within ventral structures  
19  
20 214 such as the hypothalamus (Fig. 1d). Manual measurement of precision registration confirmed these  
21  
22 215 findings: ANTs registration using values that avoided noticeable morphological distortion showed similar  
23  
24 216 MLDs to images registered using CMTK (Table 2).

25  
26 217  
27 218 We next tested whether these registration parameters also improved precision for the co-aligned  
28  
29 219 transgenic lines. For ZBB, we co-scanned transgene and enhancer trap expression patterns with the  
30  
31 220 *vglut2a:dsRed* transgene, allowing us to register each expression pattern to *vglut2a*<sub>ZBB</sub>. We first compared  
32  
33 221 the overlap and morphology of the Mauthner cells from brain scans of three different individuals of  
34  
35 222 transgenic line *J1229aGt* [23]. Overlap of Mauthner cell bodies was similar for CMTK and ANTs (Fig.  
36  
37 223 1e,f). However, in CMTK registered images, the Mauthner axon was distorted in the caudal medulla,  
38  
39 224 whereas axon morphology was preserved with ANTs. Second, in our previous work, we assessed the  
40  
41 225 precision of CMTK registration using line *y339Et* by independently scanning two sets of three larvae,  
42  
43 226 producing an average for each set, and visually comparing the result. With CMTK we had noted  
44  
45 227 misalignment of approximately 1 cell diameter in the neuropil of the optic tectum (Fig. 1g). This was  
46  
47 228 substantially improved with ANTs, where there was much closer alignment of the two averages (Fig. 1h).  
48  
49 229 For quantification we calculated the cross correlation for 8 landmarks within the *y339Et* pattern, and  
50  
51 230 found that the mean increased from 0.52 with CMTK to 0.63 with ANTs.

### 52 231 53 232 **Improved precision of ZBB after registration using ANTs**

54 233  
55 234 Based on the improved registration precision and reduced distortion of cell morphology achieved using  
56  
57 235 SyN, we recompiled ZBB using ANTs for registration to create a more accurate atlas (unprocessed and  
58  
59 236 registered brain images are available from [34]). We used ANTs to register the entire set of 354 brain  
60  
61 237 scans that were part of ZBB, then as before, averaged multiple larvae to create a representation of each  
62  
63 238 transgenic line, masked the average stacks to remove expression outside the brain and re-imported the  
64  
65



1  
2  
3  
4 239 resulting images into our Brain Browser software. We refer to this new recompilation of our atlas as  
5  
6 240 ZBB<sub>1.2</sub>.  
7  
8 241  
9 242 To determine whether ZBB<sub>1.2</sub> was a quantitative improvement over ZBB, we calculated a cross-  
10  
11 243 correlation score for each pattern in the browser. To avoid manually defining landmarks for each line, we  
12  
13 244 instead computationally identified three regions inside each pattern with strong expression to serve as  
14  
15 245 landmarks. For each of these regions, we iteratively performed pair-wise cross-correlations between all  
16  
17 246 individual brains from the same transgenic line, allowing us to calculate a mean cross-correlation (MCC)  
18  
19 247 value for each line. We performed this procedure first for brains registered using CMTK, then for the  
20  
21 248 same set of brains registered using ANTs, allowing us to compare MCCs for the two methods (Fig. 2a).  
22  
23 249 Overall, the correlations increased slightly from ZBB to ZBB<sub>1.2</sub> ( $0.32 \pm 0.02$  to  $0.34 \pm 0.02$ ; paired t-test  
24  
25 250  $p=0.15$ ). Although this was not statistically significant, it was instructive to examine instances with large  
26  
27 251 changes in mean cross correlation. Line *y332Et* labels a small set of cells with a salt and pepper pattern in  
28  
29 252 the right habenula. Here, cross correlation was greater after registration with CMTK (CMTK, 0.50;  
30  
31 253 ANTs 0.39), due at least in part to greater distortion of cells resulting in increased overlap between  
32  
33 254 individual fish despite the biological variability (Fig. 2b). In *y341Et*, distortion artifacts also appeared to  
34  
35 255 account for the large increase in MCC obtained with ANTs (CMTK, 0.19; ANTs 0.58). Here, cells in the  
36  
37 256 caudal hypothalamus had an elongated morphology after registration with CMTK, often stretching  
38  
39 257 outside the boundaries of the nucleus. Consequently, in this case distortion reduced rather than increased  
40  
41 258 the cross correlation score (Fig. 2c).  
42  
43 259  
44 260 Additionally, we inspected regions of ZBB<sub>1.2</sub> where we had noticed poor registration precision or  
45  
46 261 pronounced cell distortion in the original ZBB. One such area was the dorsal thalamus, where cell  
47  
48 262 morphology was noticeably perturbed after elastic registration with CMTK, with cell somas stretching  
49  
50 263 across the midline (Fig. 2d). In ZBB<sub>1.2</sub> cells retained a rounded morphology with distinct cell clusters on  
51  
52 264 the left and right sides of the brain (Fig. 2e). Similarly, distortions in cell shape that were apparent in the  
53  
54 265 caudal hypothalamus in ZBB, were absent in ZBB<sub>1.2</sub> (Fig. 2f,g). In the caudolateral medulla, we  
55  
56 266 previously obtained poor registration, with expression extending to regions outside the neural tube (Fig.  
57  
58 267 2h). In ZBB<sub>1.2</sub>, patterns had improved bilateral symmetry and were correctly confined to the neural tube  
59  
60 268 (Fig. 2i). Finally, we noticed that the posterior commissure was poorly aligned between larvae leading to  
61  
62 269 a defasciculated appearance in ZBB (Fig. 2j), whereas this tract had the correct tightly bundled  
63  
64 270 appearance in ZBB<sub>1.2</sub> (Fig. 2k).  
65  
66 271

1  
2  
3  
4  
5  
6  
7  
8  
9  
10  
11  
12  
13  
14  
15  
16  
17  
18  
19  
20  
21  
22  
23  
24  
25  
26  
27  
28  
29  
30  
31  
32  
33  
34  
35  
36  
37  
38  
39  
40  
41  
42  
43  
44  
45  
46  
47  
48  
49  
50  
51  
52  
53  
54  
55  
56  
57  
58  
59  
60  
61  
62  
63  
64  
65

272 Together, these observations confirm that ZBB<sub>1.2</sub> is a more faithful representation of the transgenic lines.  
273 Not only is cell morphology better preserved, but metrics of global registration precision as measured by  
274 mean cross correlation are nevertheless improved from those of the original ZBB atlas.

### 276 **Optimization of ANTs registration parameters for fixed tissue**

277  
278 The Z-Brain atlas was derived by registering brain scans to a single brain that was fixed, permeabilized  
279 and immunostained for tERK expression. We therefore presumed that tERK would be a useful channel  
280 for bridging the two atlases, if we could first successfully register a tERK stained *vglut2a:DsRed*  
281 expressing brain to ZBB<sub>1.2</sub>. Therefore, we fixed and co-stained a transgenic *vglut2a:DsRed* larva for  
282 DsRed and tERK, and registered the tERK pattern to ZBB<sub>1.2</sub> using the *vglut2a* pattern. We used the  
283 resulting image as our ZBB tERK reference brain (tERK<sub>ZBB</sub>; file *terk-ref-02.nii.gz* available from [32]).

284  
285 In addition to the tERK reference brain, Z-Brain contains an average of 197 tERK stained larvae, which  
286 we thought might serve as a bridge between atlases. During studies on pERK-based activity mapping, we  
287 had generated a dataset of 167 tERK stained brains and sought to use these to create an average tERK  
288 representation by registering them to tERK<sub>ZBB</sub>. However, during this process, we noticed a high degree of  
289 variability between tERK stained brains, most notably in either poor labeling of ventral brain structures or  
290 in deformation of the optic tectum neuropil. Immunohistochemistry for tERK proved highly sensitive to  
291 staining parameters with the trypsin activity, permeabilization duration, and antigen retrieval having the  
292 strongest effects. This variability was most apparent in the optic tectum, where high trypsin activity  
293 tended to disrupt morphology and reduce the volume of the tectal neuropil (Fig. 3a,b). These local  
294 distortions were not corrected by deformable image registration: alignment to tERK<sub>ZBB</sub> with the same  
295 parameters optimized for live *vglut2a* based registration, failed to correct the reduced tectal neuropil  
296 volume (Fig. 3c,d ; asterisk) and often created an artifact where the neuropil zone failed to abut the  
297 underlying cellular layer labeled by *vglut2a* expression (Fig. 3c,d ; arrowheads).

298  
299 We therefore varied the registration parameters that were optimal for live *vglut2a* registration, to find  
300 settings that best rectified the variable tissue morphology following fixation and permeabilization. For  
301 tERK registration optimization, we used a set of 6 tERK stained brains including the Z-Brain tERK  
302 reference. We iteratively varied parameters for registration to tERK<sub>ZBB</sub> and calculated the mean cross-  
303 correlation between each of the aligned tERK stains and tERK<sub>ZBB</sub> (e.g., Fig. 3e,f). Again when visually  
304 inspected, we noted a trade-off between the quality of global alignment and local distortion artifacts, with  
305 the parameters which yielded the greatest increase in MCC often producing abnormally elongated cell

1  
2  
3  
4 306 profiles throughout the brain (Fig. 3g). However, visual inspection confirmed that parameters which  
5  
6 307 increased MCC for fixed tissue greatly improved the morphology of the optic tectum neuropil (Fig. 3h,i).  
7  
8 308 We therefore used ANTs with the fixed brain parameters (Table 1, **fixed registration**) to register 167  
9  
10 309 tERK stained brains to tERK<sub>ZBB</sub>, and generated an average tERK representation comparable to the Z-  
11 310 Brain tERK average (Fig. 3j,k).  
12  
13 311

### 14 312 **Inter-atlas registration using multi-channel diffeomorphic transformation**

15 313  
16 314 By chance, both Z-Brain and ZBB incorporated seven additional gene or transgene expression patterns  
17 315 that we judged were sufficiently similar to act either as templates for bridging the datasets or to provide  
18 316 metrics for assessing the precision of a bridging registration (Table 3). For example, *vglut2a*<sub>ZBB</sub> is a  
19 317 confocal scan of DsRed in a single larva from transgenic line *TgBAC(slc17a6b:loxP-DsRed-loxP-*  
20 318 *GFP)nns14*, whereas Z-Brain includes *Tg(slc17a6:EGFP)zf139*. In both cases, reporter expression is  
21 319 regulated by the same bacterial artificial chromosome [15,20]. Crossing these two lines allowed us to scan  
22 320 DsRed and EGFP in the same larva and confirm that the patterns were largely congruous, potentially  
23 321 allowing us to use *vglut2a* expression to bridge the two atlases. Likewise, the expression patterns of  
24 322 *tERK*, *elavl3*, *isl2b*, *vmat2* in Z-Brain and ZBB appeared sufficiently similar to provide templates for atlas  
25 323 co-registration.  
26 324

27 325 We used seven expression patterns to evaluate registration precision using cross correlation: *vglut2a*,  
28 326 *isl2b*, *vmat2*, *elavl3*, *isl1*, *gad1b* and *glyT2*. For each pattern we identified a set of 5-18 landmarks that  
29 327 were widely distributed to represent diverse brain regions. For each landmark, we measured the cross-  
30 328 correlation between the corresponding volumes in ZBB and Z-Brain. We then calculated the mean of all  
31 329 cross correlation (MCC) values for landmarks associated with a given expression pattern. We used two  
32 330 measures of registration precision. The first metric ( $M_1$ ) was the mean of the MCCs for *isl1*, *gad1b* and  
33 331 *glyT2* expression patterns in ZBB and in Z-Brain after registration to ZBB. These three expression  
34 332 patterns do not provide sufficient coverage across all brain regions to use for registration, but served as  
35 333 independent channels to estimate registration precision. However, as these patterns are relatively sparse  
36 334 they do not comprehensively assess precision across all brain regions. To provide a global measure of  
37 335 precision, we therefore also used a second metric ( $M_2$ ) that was the mean of all seven MCCs: those in  $M_1$   
38 336 plus four of the patterns used as references for registration - *vglut2a*, *tERK*, *isl2b* and *vmat2*. Although  $M_2$   
39 337 uses expression patterns that together provide good coverage for the entire brain, we expected that the  
40 338 four patterns that were also used to guide the deformable registration, would artificially inflate the MCC.  
41 339

1  
2  
3  
4 340 We first used CMTK to register Z-Brain to ZBB<sub>1,2</sub>. Maximal M<sub>1</sub> and M<sub>2</sub> scores were obtained using the  
5  
6 341 average *vglut2a* pattern as the reference (Fig. 4a). We therefore registered all images in Z-Brain to ZBB  
7  
8 342 using the *vglut2a* average in each dataset as the reference channel. We observed severe tissue distortions  
9  
10 343 in several brain regions, with noticeable flattening of the torus longitudinalis and gross tissue distortions,  
11 344 particularly in ventral brain regions (Fig. 4b,c; ZBrain-CMTK).

12 345  
13  
14 346 Next, for comparison, we used the ANTs SyN algorithm to register the atlases. Ideally, patterns for  
15  
16 347 registration should include information throughout the brain. Because ANTs can use multiple concurrent  
17  
18 348 reference channels to derive an optimal transformation matrix, we speculated that the best possible  
19 349 transformation would be achieved by a combination of channels with complementary information. We  
20  
21 350 therefore produced an inter-atlas transformation matrix using every combination of the *elavl3*, *isl2b*,  
22 351 *vglut2a*, *vmat2*, *tERK<sub>REF</sub>* (tERK single brain) and *tERK<sub>AV</sub>* (tERK average brain) patterns as references. As  
23  
24 352 Z-Brain used fixed samples, we used the registration parameters previously optimized for the greater  
25  
26 353 variability present in fixed tissue. Multi-channel registration significantly improved M<sub>1</sub> and M<sub>2</sub> values  
27  
28 354 compared to any single channel alone and to transformations obtained using CMTK. The registration  
29 355 obtained with *vglut2a*, *tERK<sub>REF</sub>*, *vmat2* and *isl2b* gave the highest M<sub>2</sub> value and an M<sub>1</sub> score within 1% of  
30  
31 356 the highest scoring combination (Fig. 4a). Moreover, the overt tissue distortions noted after elastic  
32  
33 357 registration with CMTK were far less salient using these parameters (Fig. 4b,c ; ZBrain-SyN). This  
34  
35 358 conclusion was supported when we assessed registration precision by visually locating landmarks in the  
36 359 *vglut2a* pattern after registration with CMTK, or multi-channel ANTs registration. After calculating the  
37  
38 360 distance from the same points in the *vglut2a<sub>ZBB</sub>* pattern we found the multi-channel ANTs registered  
39 361 points were on average 9.9 μm away from the reference points, compared to 17.9 μm for CMTK (Table  
40  
41 362 4). We therefore applied the transformation matrix obtained with this set of channels to the database of  
42  
43 363 gene expression patterns in Z-Brain to align them to ZBB<sub>1,2</sub>.

44 364  
45  
46 365 The precision of the inter-atlas registration is apparent when comparing the location of cells that are  
47  
48 366 present in both datasets, such as those labeled by *Pet1:GFP*. The Z-Brain transformed pattern closely  
49 367 matches the transgene expression pattern in ZBB<sub>1,2</sub> within the superior raphe (Fig. 4d — note however  
50  
51 368 that unexpectedly, the line in ZBB<sub>1,2</sub> also labels a set of more rostral cells not apparent in Z-Brain). Both  
52  
53 369 atlases also include lines labeling the Mauthner cells. After registration, Mauthner cells in the atlases  
54  
55 370 substantially overlapped, although they were several microns more medially positioned in ZBB<sub>1,2</sub> (Fig.  
56 371 4e). Similarly, we used the inverse of the transformation generated by SyN to register ZBB<sub>1,2</sub> to the Z-  
57  
58 372 Brain coordinate system. As expected, expression in the *DAT:GFP* line in ZBB<sub>1,2</sub> overlapped well with  
59 373 the tyrosine hydroxylase stain from Z-Brain in the pretectum (Fig. 4f), although again, the ZBB<sub>1,2</sub> pattern

1  
2  
3  
4 374 was slightly more medial than in Z-Brain. More caudally, the *glyT2:GFP* transgenic line labels  
5  
6 375 glycinergic neurons in longitudinal columns in the medulla oblongata [35]. These columns were closely  
7  
8 376 aligned after ZBB<sub>1.2</sub> was registered to Z-Brain (Fig. 4g). Although best practice is to align directly to  
9  
10 377 either ZBB or Z-Brain, because many researchers will have already registered data sets to either ZBB or  
11 378 Z-Brain, or for cases where it may not be possible to directly register a dataset, we have provided  
12  
13 379 transformation matrixes and detailed instructions to quickly re-align datasets to either of the coordinate  
14 380 systems ([36] ; instructions are provided in Additional File 2).  
15  
16 381  
17 382 Z-Brain includes 294 masks that represent anatomically defined brain regions or discrete clusters of cells  
18 383 present in transgenic lines. We selected 113 of these masks that delineate neuroanatomical regions and  
19 384 transformed them into the ZBB<sub>1.2</sub> coordinate system. We had previously defined a small number of our  
20 385 own anatomical masks by thresholding clusters of neuronal cell bodies located in well-defined brain  
21 386 regions. In contrast, the Z-Brain masks are more comprehensive, have smoother boundaries and include  
22 387 both the cell bodies and neuropil for a given region (Fig. 4h-k). We therefore imported the Z-Brain masks  
23 388 into ZBB<sub>1.2</sub>, replacing most of our existing masks. We also modified the *Brain Browser* software to  
24 389 automatically report the neuroanatomical identity of a selected pixel, or to display the boundaries of the  
25 390 region encompassing a selected point. The updated software and rebuilt database in ZBB<sub>1.2</sub> can be  
26 391 downloaded from our website [37].  
27  
28 392  
29  
30 393 Finally, as the Zebrafish Brain Browser's strength is primarily in two dimensions (i.e., the visualization of  
31 394 horizontal, transverse, and sagittal slices through the brain), we decided to develop interactive tools to  
32 395 better facilitate three dimensional exploration. The use of 3D graphics to represent complex structure can  
33 396 also provide a more intuitive sensory experience that avoids cognitive bias or misinterpretation  
34 397 inadvertently introduced by sometimes largely arbitrary two dimensional reductions [38,39]. By taking  
35 398 advantage of stereoscopy and vestibular-enhanced parallax (head tracking), the more immersive and  
36 399 holistic experience of Virtual Reality (VR) can also significantly improve performance of basic tasks like  
37 400 searching and making comparisons [40,41]. We therefore implemented our Zebrafish Brain Browser in  
38 401 both an open Web3D platform (X3D) and a custom game engine (Unity). First, we converted masks  
39 402 representing anatomical regions to meshes and built a Web3D interface using X3D to inspect the spatial  
40 403 relationship between different brain regions (Fig. 5a,b)[42]. Users can navigate within the brain using any  
41 404 web browser, rotating and zooming into brain regions to better interrogate larval neuroanatomy. Second,  
42 405 using the Unity platform we wrote a VR app to view the brain and neuroanatomical regions. By running  
43 406 the app on a cell phone, and inserting it into an inexpensive Google cardboard viewer, users can 'walk  
44  
45  
46  
47  
48  
49  
50  
51  
52  
53  
54  
55  
56  
57  
58  
59  
60  
61  
62  
63  
64  
65

1  
2  
3  
4 407 into' the brain, and see from the inside the inter-relationship between neuroanatomical domains (Fig. 5c,d)  
5  
6 408 [43].  
7  
8 409

## 9 410 **Discussion**

10 411  
11  
12 412 Digitized data-derived brain atlases provide an opportunity to continuously integrate new information and  
13  
14 413 iteratively improve data accuracy within a common spatial framework. Thus, as methods evolve and  
15  
16 414 technology improves, new insights can be easily added to existing data to provide an increasingly rich  
17  
18 415 view of brain structure and function. Because the entire larval zebrafish brain can be rapidly imaged at  
19  
20 416 cellular resolution, it is possible to envisage an atlas that combines detailed information on cell type  
21  
22 417 (including gene expression and morphology), connectivity and activity under a variety of different  
23  
24 418 physiological conditions. At present, biological variability presents an obstacle, as brain regions contain  
25  
26 419 multiple intermingled cell types that are not positioned in precisely the same manner between larvae. To  
27  
28 420 circumvent this in the existing zebrafish brain atlases, multiple individuals of a given line are sampled and  
29  
30 421 averaged to generate a representative expression pattern. Current atlases are thus essentially heat maps of  
31  
32 422 gene expression or activity. Despite this spatial ambiguity, aggregating information from different sources  
33  
34 423 into the same spatial framework still provides valuable indicators of cell type, gene co-expression, and  
35  
36 424 neural activity under defined conditions.  
37

38 425  
39 426 Ideally different atlas projects might use the same reference brain, however in practice the choice of a  
40  
41 427 reference is dictated by study-specific experimental requirements. For example, despite the deformations  
42  
43 428 introduced by fixation and permeabilization, a fixed brain is essential for activity mapping using pERK  
44  
45 429 immunohistochemistry. In contrast, we were able to take advantage of the optical transparency of larvae  
46  
47 430 to rapidly scan and register several hundred individuals representing more than 100 different transgenic  
48  
49 431 lines. For our purposes, the *TgBAC(slc17a6b:loxP-DsRed-loxP-GFP)nns14* line was ideal, because  
50  
51 432 through Cre injection, we generated a *vglut2a:GFP* line with an almost identical pattern, allowing us to  
52  
53 433 co-register lines with either GFP or RFP fluorescence. However, we have also used pan-neuronal  
54  
55 434 Cerulean or mCardinal as a reference channel when the green and red channels both contained useful  
56  
57 435 information on transgene expression. Our work now demonstrates that it is feasible to contribute to  
58  
59 436 community efforts at building an integrated map of brain structure, expression and activity, while  
60  
61 437 allowing reference image selection to be guided by technical considerations.  
62

63 438  
64 439 One caveat to this conclusion is that deformable image registration can easily introduce artifacts into cell  
65 440 morphology if parameters are not carefully monitored and constrained. Indeed, a special challenge for

1  
2  
3  
4  
5  
6  
7  
8  
9  
10  
11  
12  
13  
14  
15  
16  
17  
18  
19  
20  
21  
22  
23  
24  
25  
26  
27  
28  
29  
30  
31  
32  
33  
34  
35  
36  
37  
38  
39  
40  
41  
42  
43  
44  
45  
46  
47  
48  
49  
50  
51  
52  
53  
54  
55  
56  
57  
58  
59  
60  
61  
62  
63  
64  
65

441 brain registration in zebrafish is preserving the local morphology of neuronal cell bodies and axons, while  
442 permitting sufficient deformation to correct for biological differences and changes in brain structure  
443 arising from tissue fixation and permeabilization. Thus, while B-spline registration with CMTK produced  
444 acceptable inter-atlas alignment, it also introduced noticeable distortions into local brain structure that  
445 affected neuronal cell morphology. Such artifacts were particularly severe in ventral brain regions such as  
446 the caudal hypothalamus, and may therefore be due to differences in ventral signal intensity between the  
447 datasets. In ZBB, in order to compensate for the increase in light diffraction with tissue depth, we  
448 systematically increased laser intensity with confocal scan progression (z-compensation). As a result, the  
449 Z-Brain and ZBB datasets are comparable in dorsal brain regions, but there is a noticeable discrepancy  
450 ventrally which may account for the loss of registration fidelity. Alternatively, although z-compensation  
451 partially corrects for reduced fluorescent intensity, there is a noticeable drop-off in image resolution in  
452 ventral regions; the resulting loss of information may lead to lower quality registration. Registration  
453 algorithms that allow parameters to vary by depth may ameliorate the effects of these physical imaging  
454 constraints.

455  
456 Nevertheless, the symmetrical diffeomorphic transformation in ANTs provides a satisfactory solution to  
457 these problems. For live tissue, we found parameters that allowed the ANTs SyN transform to achieve  
458 similar or better registration precision than previously achieved using CMTK, while minimizing overt  
459 distortions in tissue structure and neuronal cell morphology. In our hands, permeabilization of fixed tissue  
460 tended to produce variable changes in neuropil structure which was most salient in the optic tectum.  
461 Specifically, neuropil volume was diminished when fresh aliquots of trypsin were used for extended  
462 durations. These artifacts can be minimized by stringent oversight of reagent viridity. However, by  
463 calibrating SyN parameters to permit larger deformations, we were able to accommodate the variability  
464 introduced in tissue processing.

465  
466 Currently, the main limitations for use of the SyN registration algorithm in ANTs are the large memory  
467 demands (73 GB for a single channel registration) and long computational times (3-5 hours for a single  
468 channel using 24 cores) required for registration of images with a resolution sufficient for the brain-wide  
469 visualization of neuronal morphology (e.g., 1000 x 600 x 350 pixels). For multi-channel registrations,  
470 memory demands and computation time were even greater: 106 GB for 6 channels taking over 16 hours  
471 on 24 cores. However, our present ANTs SyN parameters likely can be further optimized to reduce these  
472 demands. For instance, our parameters currently include 10 iterations of transformation matrix  
473 optimization at full image resolution. From our experience, these full resolution registration cycles do not  
474 significantly improve cross correlation scores, but greatly increase computation time. Thus, computation

1  
2  
3  
4 475 time may be reduced by adjusting registration resolution as well as other parameters without adversely  
5  
6 476 affecting registration quality. Although computational resources did not present a bottleneck for  
7  
8 477 registering a small number of samples, this increase in the demands of a single registration made it  
9  
10 478 difficult to optimize registration parameters as extensively as we had done previously with CMTK [1].  
11 479 For example, during our initial effort to optimize registration parameters for live *vglut2a* expression, we  
12  
13 480 used a single representative example rather than assessing parameters for a set of several independent  
14  
15 481 scans. By reducing computation time, we would be able to explore more comprehensively the parameter  
16  
17 482 space available with SyN and evaluate alternative diffeomorphic transforms available with ANTs that  
18  
19 483 may provide still better registration fidelity.

20  
21 485 An obstacle to systematically calibrating registration parameters was finding a suitable metric to  
22  
23 486 quantitatively evaluate registration precision. This is a recognized problem, and it is not clear that a  
24  
25 487 general solution exists [33]. We used cross-correlation within localized image neighborhoods that  
26  
27 488 included relatively high contrast internal image boundaries. However in registering live *vglut2a:DsRed*  
28  
29 489 image stacks, we found that the highest scoring transformations achieved accurate global brain alignment  
30  
31 490 at the expense of biologically plausible cell morphology. Therefore, it was essential to visually compare  
32  
33 491 the output of every transformation and make subjective judgments about registration quality. This was  
34  
35 492 difficult, because distortions, when present, tended to be variable in different parts of the image, thus  
36  
37 493 requiring the entire image stack produced by each transformation to be scrutinized to select optimal  
38  
39 494 parameter settings.

40  
41 495  
42  
43 496 Nevertheless, this study demonstrates that the ANTs diffeomorphic symmetric normalization algorithm  
44  
45 497 improves upon elastic registration for precise registration of whole brain images in larval zebrafish and is  
46  
47 498 markedly better at preserving neuronal cell morphology. By systematically testing SyN registration  
48  
49 499 parameters for registering images acquired using live scans, we improved the ZBB atlas. Then, after  
50  
51 500 calibrating registration parameters for fixed tissue and using multi-channel optimization, we were able to  
52  
53 501 align the Z-Brain atlas into the ZBB coordinate space, and vice-versa. We believe that integrating the  
54  
55 502 information present in each of these atlases produces a richer framework for future studies of structural  
56  
57 503 and functional relationships within the nervous system. Large digital datasets such as those present in  
58  
59 504 brain atlases can be used for many types of bioinformatic analysis. Z-Brain and ZBB already include  
60  
61 505 software that can be used to explore the larval zebrafish brain, and we hope that by integrating these  
62  
63 506 datasets into a single coordinate system, we will help to stimulate the development of additional  
64  
65 507 computational tools and methods for querying this information.

60  
61 508



1  
2  
3  
4  
5  
6  
7  
8  
9  
10  
11  
12  
13  
14  
15  
16  
17  
18  
19  
20  
21  
22  
23  
24  
25  
26  
27  
28  
29  
30  
31  
32  
33  
34  
35  
36  
37  
38  
39  
40  
41  
42  
43  
44  
45  
46  
47  
48  
49  
50  
51  
52  
53  
54  
55  
56  
57  
58  
59  
60  
61  
62  
63  
64  
65

**509 Availability of supporting data**

510  
511 All individual brain scans, both before and after registration to a ZBB reference brain, are available in the  
512 *GigaScience* repository, GigaDB [34]. The GigaDB repository also includes the set of reference brains  
513 used for ZBB [32] and the transformation matrices used to convert between ZBB and Z-Brain coordinate  
514 systems [36].

**516 Abbreviations**

- 517
- 518 ac, anterior commissure
- 519 DT, Thalamus
- 520 GT, Griseum tectale
- 521 Ha, Habenula
- 522 Hc, Hypothalamus caudal zone
- 523 Hi, Hypothalamus intermediate zone
- 524 MO, Medulla oblongata
- 525 NXm, Vagus motor neurons
- 526 OB, Olfactory bulb
- 527 OE, Olfactory epithelium
- 528 IO, Inferior olive
- 529 LC, Locus coeruleus
- 530 MN, Mauthner neuron
- 531 MO, Medulla oblongata
- 532 Pal, Pallium
- 533 pc, posterior commissure
- 534 Pr, Pretectum
- 535 SR, Superior raphe
- 536 Teg, Tegmentum
- 537 TeOn, Optic tectum neuropil
- 538 TG, Trigeminal ganglion
- 539 TL, Torus longitudinalis

540  
541  
**542 Competing Interests**

543  
544 The authors declare that they have no competing interests.

**546 Authors' Contribution**

547  
548 GDM and HAB conceived the experiments. GDM, KMT, EJH and HAB optimized ANTS for zebrafish  
549 brain registration. GDM, MB and AKG contributed confocal brain scans and generated meshes. NFP

1  
2  
3  
4  
5  
6  
7  
8  
9  
10  
11  
12  
13  
14  
15  
16  
17  
18  
19  
20  
21  
22  
23  
24  
25  
26  
27  
28  
29  
30  
31  
32  
33  
34  
35  
36  
37  
38  
39  
40  
41  
42  
43  
44  
45  
46  
47  
48  
49  
50  
51  
52  
53  
54  
55  
56  
57  
58  
59  
60  
61  
62  
63  
64  
65

developed the X3D/HTML5 based browser. DDN developed the Unity VR browser. GDM and HAB wrote the manuscript. All authors approved the final manuscript.

## Acknowledgements

This work was supported by the Intramural Research Program of the Eunice Kennedy Shriver National Institute for Child Health and Human Development (NICHD) and utilized the high-performance computational capabilities of the Biowulf Linux cluster at the National Institutes of Health, Bethesda, MD [44]. We thank Owen Randlett for valuable discussion and help checking the correspondence of *vglut2a* expression patterns. We are grateful to Sinisa Pajevic (NIH/CIT) for advice on computational procedures and to M. Okan Irfanglu and Neda Sadeghi (NICHD) for guidance in optimizing ANTs parameters.

## References

1. Marquart GD, Tabor KM, Brown M, *et al.* A 3D Searchable Database of Transgenic Zebrafish Gal4 and Cre Lines for Functional Neuroanatomy Studies. *Front Neural Circuits* 2015; **9**:78.
2. Randlett O, Wee CL, Naumann EA, *et al.* Whole-brain activity mapping onto a zebrafish brain atlas. *Nat Methods* 2015; **12**:1039–1046.
3. Ronneberger O, Liu K, Rath M, *et al.* ViBE-Z: a framework for 3D virtual colocalization analysis in zebrafish larval brains. *Nat Methods* 2012; **9**:735–42.
4. Rath M, Nitschke R, Filippi A, Ronneberger O, Driever W. Generation of high quality multi-view confocal 3D datasets of zebrafish larval brains suitable for analysis using Virtual Brain Explorer (ViBE-Z) software. 2012. <http://dx.doi.org/10.1038/protex.2012.031> (last accessed, 24 March 2017)
5. Portugues R, Feierstein CE, Engert F, Orger MB. Whole-Brain Activity Maps Reveal Stereotyped, Distributed Networks for Visuomotor Behavior. *Neuron* 2014; **81**:1328–1343.
6. Rohlfing T, Maurer CR Jr. Nonrigid image registration in shared-memory multiprocessor environments with application to brains, breasts, and bees. *IEEE Trans Inf Technol Biomed* 2003; **7**:16–25.
7. Avants BB, Epstein CL, Grossman M, Gee JC. Symmetric diffeomorphic image registration with cross-correlation: Evaluating automated labeling of elderly and neurodegenerative brain. *Med Image Anal* 2008; **12**:26–41.
8. Avants BB, Tustison NJ, Song G, Cook PA, Klein A, Gee JC. A reproducible evaluation of ANTs similarity metric performance in brain image registration. *NeuroImage* 2011; **54**:2033–2044.
9. Higashijima S, Hotta Y, Okamoto H. Visualization of cranial motor neurons in live transgenic zebrafish expressing green fluorescent protein under the control of the islet-1 promoter/enhancer. *J Neurosci* 2000; **20**:206–18.

1  
2  
3  
4 585 10. Wen L, Wei W, Gu W, *et al.* Visualization of monoaminergic neurons and neurotoxicity of MPTP in  
5 586 live transgenic zebrafish. *Dev Biol* 2008; **314**:84–92.  
6  
7 587 11. Xi Y, Yu M, Godoy R, Hatch G, Poitras L, Ekker M. Transgenic zebrafish expressing green  
8 588 fluorescent protein in dopaminergic neurons of the ventral diencephalon. *Dev Dyn* 2011; **240**:2539–47.  
9  
10 589 12. Lillesaar C, Stigloher C, Tannhauser B, Wullimann MF, Bally-Cuif L. Axonal projections originating  
11 590 from raphe serotonergic neurons in the developing and adult zebrafish, *Danio rerio*, using transgenics to  
12 591 visualize raphe-specific *pet1* expression. *J Comp Neurol* 2009; **512**:158–82.  
13  
14  
15 592 13. Tabor KM, Bergeron SA, Horstick EJ, *et al.* Direct activation of the Mauthner cell by electric field  
16 593 pulses drives ultra-rapid escape responses. *J Neurophysiol* 2014; **112**:834–844.  
17  
18 594 14. Scott EK, Baier H. The cellular architecture of the larval zebrafish tectum, as revealed by *gal4*  
19 595 enhancer trap lines. *Front Neural Circuits* 2009; **3**:13.  
20  
21 596 15. Satou C, Kimura Y, Hirata H, Suster ML, Kawakami K, Higashijima S. Transgenic tools to  
22 597 characterize neuronal properties of discrete populations of zebrafish neurons. *Development* 2013;  
23 598 **140**:3927–31.  
24  
25 599 16. McLean DL, Fan J, Higashijima S, Hale ME, Fetcho JR. A topographic map of recruitment in spinal  
26 600 cord. *Nature* 2007; **446**:71–5.  
27  
28 601 17. Pittman AJ, Law MY, Chien CB. Pathfinding in a large vertebrate axon tract: isotopic interactions  
29 602 guide retinotectal axons at multiple choice points. *Development* 2008; **135**:2865–71.  
30  
31 603 18. Yokogawa T, Hannan MC, Burgess HA. The dorsal raphe modulates sensory responsiveness during  
32 604 arousal in zebrafish. *J Neurosci* 2012; **32**:15205–15215.  
33  
34 605 19. Satou C, Kimura Y, Higashijima S. Generation of multiple classes of V0 neurons in zebrafish spinal  
35 606 cord: progenitor heterogeneity and temporal control of neuronal diversity. *J Neurosci* 2012; **32**:1771–83.  
36  
37 607 20. Bae YK, Kani S, Shimizu T, *et al.* Anatomy of zebrafish cerebellum and screen for mutations  
38 608 affecting its development. *Dev Biol* 2009; **330**:406–26.  
39  
40 609 21. Fosque BF, Sun Y, Dana H, *et al.* Labeling of active neural circuits in vivo with designed calcium  
41 610 integrators. *Science* 2015; **347**:755–760.  
42  
43 611 22. Nechiporuk A, Linbo T, Poss KD, Raible DW. Specification of epibranchial placodes in zebrafish.  
44 612 *Development* 2007; **134**:611–623.  
45  
46 613 23. Burgess HA, Johnson SL, Granato M. Unidirectional startle responses and disrupted left-right co-  
47 614 ordination of motor behaviors in *robo3* mutant zebrafish. *Genes Brain Behav* 2009; **8**:500–11.  
48  
49 615 24. Inoue D, Wittbrodt J. One for All—A Highly Efficient and Versatile Method for Fluorescent  
50 616 Immunostaining in Fish Embryos. *PLOS ONE* 2011; **6**:e19713.  
51  
52 617 25. Schneider CA, Rasband WS, Eliceiri KW. NIH Image to ImageJ: 25 years of image analysis. *Nat*  
53 618 *Methods* 2012; **9**:671–675.  
54  
55 619 26. Williams G. *NIfTi Input/Output*. <https://imagej.nih.gov/ij/plugins/nifti.html> (last accessed, 22 March  
56 620 2017)  
57  
58  
59  
60  
61  
62  
63  
64  
65

1  
2  
3  
4 621 27. Heisenberg M, Schmid B. *IntSeg 3D*. [http://3dviewer.neurofly.de/IntSeg\\_3D](http://3dviewer.neurofly.de/IntSeg_3D) (last accessed, 22 March  
5 622 2017)  
6  
7 623 28. Web3D Consortium. *Open Standards for Real-Time 3D Communication*. <http://www.web3d.org/> (last  
8 624 accessed, 22 March 2017)  
9  
10  
11 625 29. Vicomtech-IK4. *AtlasConversionScripts*. <https://github.com/VolumeRC/AtlasConversionScripts> (last  
12 626 accessed, 22 March 2017)  
13  
14 627 30. Klein A, Andersson J, Ardekani BA, *et al*. Evaluation of 14 nonlinear deformation algorithms applied  
15 628 to human brain MRI registration. *NeuroImage* 2009; **46**:786–802.  
16  
17 629 31. Murphy K, Ginneken B van, Reinhardt JM, *et al*. Evaluation of Registration Methods on Thoracic  
18 630 CT: The EMPIRE10 Challenge. *IEEE Trans Med Imaging* 2011; **30**:1901–1920.  
19  
20  
21 631 32. *ZBB Reference Brains*. [http://helix.nih.gov/~BurgessLab/reference\\_brains.zip](http://helix.nih.gov/~BurgessLab/reference_brains.zip) (last accessed, 22 March  
22 632 2017) To be replaced with GigaDB DOI upon publication  
23  
24 633 33. Rohlfing T. Image Similarity and Tissue Overlaps as Surrogates for Image Registration Accuracy:  
25 634 Widely Used but Unreliable. *IEEE Trans Med Imaging* 2012; **31**:153–163.  
26  
27 635 34. *ZBB Raw and Registered Brain Images* GigaDB DOI to be provided upon publication  
28  
29 636 35. Kinkhabwala A, Riley M, Koyama M, *et al*. A structural and functional ground plan for neurons in the  
30 637 hindbrain of zebrafish. *Proc Natl Acad Sci U A* 2011; **108**:1164–9.  
31  
32  
33 638 36. *ZBB-ZBrain Transformation Matrices*. <https://helix.nih.gov/~BurgessLab/zbb-zbrain.zip> (last  
34 639 accessed, 22 March 2017) To be replaced with GigaDB DOI upon publication  
35  
36 640 37. *Zebrafish Brain Browser*. <https://science.nichd.nih.gov/confluence/display/burgess/Brain+Browser>  
37 641 (last accessed, 22 March 2017)  
38  
39 642 38. Ota D, Loftin B, Saito T, Lea R, Keller J. Virtual reality in surgical education. *Comput Biol Med*  
40 643 1995; **25**:127–137.  
41  
42 644 39. Ware C, Franck G. Viewing a graph in a virtual reality display is three times as good as a 2D diagram.  
43 645 In: *Proceedings of 1994 IEEE Symposium on Visual Languages.*; 1994:182–183.  
44  
45  
46 646 40. Bowman DA, McMahan RP. Virtual Reality: How Much Immersion Is Enough? *Computer* 2007;  
47 647 **40**:36–43.  
48  
49 648 41. Henry JAG, Polys NF. The effects of immersion and navigation on the acquisition of spatial  
50 649 knowledge of abstract data networks. *Procedia Comput Sci* 2010; **1**:1737–1746.  
51  
52  
53 650 42. *Zebrafish Anatomy Explorer*.  
54 651 <http://metagrid2.sv.vt.edu/~npolys/NIH/Burgess/ZebraFishBrowser/ZebrafishBrowser.html> (last  
55 652 accessed, 22 March 2017)  
56  
57 653 43. *Virtual reality brain browser*.  
58 654 <https://science.nichd.nih.gov/confluence/display/burgess/Brain+Browser#BrainBrowser-vrfishbrain> (last  
59 655 accessed, 22 March 2017)  
60  
61  
62  
63  
64  
65

1  
2  
3  
4 656 44. *High Performance Computing at the NIH*. 2016. <https://hpc.nih.gov> (last accessed, 22 March 2017)  
5  
6 657

7  
8 658 **Figure legends**  
9

10 659  
11 660 **Table 1. ANTs command parameters for image registration**  
12

13 661  
14 662 **Table 2. Registration precision for CMTK, ANTs (using parameters for optimal mean cross**  
15 **correlation), and ANTs (using parameters that minimize distortion), as measured by manually**  
16 **locating landmarks within the image.**  
17

18 664  
19 665 Values are distances in microns from the corresponding landmarks in the reference brain. Three experts  
20 666 located, blind to the identity of the samples, located the landmarks in each registered image. The distance  
21 667 shown is the mean of the three distances from the same landmarks in the reference brain. To assess  
22 668 reproducibility of locating landmarks in the reference brain, the same three people also located the  
23 669 landmarks in the reference brain (fourth column) demonstrating that these landmarks can be located by  
24 670 experts to within 5 microns.  
25  
26  
27  
28  
29

30 671  
31 672 **Table 3. Brain images in ZBB and Z-Brain that were used as templates for registration and/or for**  
32 **measurement of registration precision.**  
33  
34

35 673  
36 674  
37 675 **Table 4. Precision of ZBB and Z-brain co-alignment after using CMTK with tERK as the**  
38 **registration channel, CMTK with *vglut:dsRed* as the registration channel or multi-channel**  
39 **registration using ANTs.**  
40

41 676 Distances (in microns) were measured as in Table 2, by three experts who were blind to the identity of the  
42 677 samples.  
43  
44

45 680  
46 681 **Figure 1. Optimization of parameters for registration of live brain scans using ANTs**

47 682 **(a)** Dorsal maximum projections through the twelve 50 x 50 x 50  $\mu$ m cubes used to calculate the mean  
48 683 cross correlation (MCC) for *vglut2a* expression patterns. Top row shows projections for the reference  
49 684 image, *vglut2a*<sub>ZBB</sub>, and bottom row shows projections for a representative *vglut2a:dsRed* brain that was  
50 685 registered to the reference brain using CMTK. Correlation coefficients are indicated in the bottom row.  
51  
52  
53 686 For this example, the MCC is the mean of the indicated values, 0.73.

54  
55 687 **(b-d)** Comparison of a single plane in *vglut2a*<sub>ZBB</sub>, and of the representative *vglut2a:dsRed* brain after  
56 688 registration using CMTK, ANTs with parameters that produced the largest mean cross correlation score  
57 689 (0.85 ; MCC optimal), and ANTs with parameters where visual inspection showed cell morphology was  
58  
59  
60  
61

1  
2  
3  
4 690 best preserved (Visual optimal. MCC was 0.81). Slices are through the optic tectum (**b**), medulla  
5  
6 691 oblongata (**c**) and hypothalamus (**d**). Distortion artifacts introduced by CMTK in the hypothalamus  
7  
8 692 (arrowhead) as well as poor cell morphology with CMTK and ANTs-MCC-optimal (arrow) are indicated.  
9  
10 693 (**e,f**) Comparison of a single horizontal plane in *J1229aGt* showing expression of GFP in the Mauthner  
11  
12 694 cell and axon (arrowheads) for three individual larvae (pseudo-colored red, green and blue). Registration  
13  
14 695 was performed with CMTK (**e**) or ANTs (**f**).  
15  
16 696 (**g,h**) Single coronal plane through the optic tectum in two separate average brain images (colored green  
17  
18 697 and magenta) for *y393Et*. For each brain image, we independently scanned three individual brains and  
19  
20 698 registered them using CMTK (**g**) or ANTs (**h**). Scale bar 100  $\mu$ m.  
21  
22 699

## 21 700 **Figure 2. Improved precision of transgene representations in ZBB<sub>1,2</sub>**

22 701 (**a**) Mean of cross-correlation values derived from all pairwise comparisons of individual brains for each  
23  
24 702 transgenic line in ZBB, after registration with CMTK and ANTs. Dotted line indicates 1:1 ratio.  
25  
26 703 (**b**) Horizontal slice through the right habenula in *y332Et*, showing three individual brain scans after  
27  
28 704 registration with CMTK (top row), and the same slices pseudo-colored (red, green blue) and  
29  
30 705 superimposed. Bottom row shows the equivalent after registration using ANTs.  
31  
32 706 (**c**) Horizontal slice through the caudal hypothalamus of three individual *y341Et* larvae as well as their  
33  
34 707 pseudo-colored superimposition following registration with CMTK (top row) or ANTs (bottom row).  
35  
36 708 (**d,e**) Horizontal slice through the thalamus showing the averaged representation of enhancer trap line  
37  
38 709 *y304Et*, where individual brains were registered with CMTK for ZBB (**d**), or by ANTs for ZBB<sub>1,2</sub> (**e**).  
39  
40 710 Arrow indicates neurons that are artificially elongated across the midline. Scale bar 100  $\mu$ m.  
41  
42 711 (**f,g**) Coronal slice through the caudal hypothalamus showing the average enhancer trap line *y269Et* brain  
43  
44 712 with CMTK (**d**) and ANTs (**e**). Scale bar 50  $\mu$ m.  
45  
46 713 (**h,i**) Coronal slice through the medulla oblongata showing the average *phox2b:GFP* brain with CMTK (**f**)  
47  
48 714 and ANTs (**g**). Scale bar 50  $\mu$ m.  
49  
50 715 (**j,k**) Horizontal projection through the posterior commissure (arrow) for the average *y351Et* brain  
51  
52 716 obtained with CMTK (**j**) or ANTs (**k**). Scale bar 100  $\mu$ m.  
53  
54 717

## 51 718 **Figure 3. Optimization of ANTs registration parameters for fixed tissue**

52 719 (**a,b**) Horizontal section through the optic tectum after immunostaining for tERK (red) and DsRed in  
53  
54 720 *vglut2a:DsRed* (green), using diluted (**a, sample A**) or fresh trypsin (**b, sample B**). Asterisk indicates  
55  
56 721 missing area of tectal neuropil due to permeabilization artifact.  
57  
58 722 (**c,d**) Registration, using the *vglut2a:DsRed* expression pattern, of the tERK immunostain (red) in same  
59  
60 723 brains as in (**a,b**) to tERK<sub>ZBB</sub> using the parameters previously optimized for live registration. White shows

1  
2  
3  
4 724 the ZBB<sub>1,2</sub> *vglut2a:dsRed* pattern. Arrowheads highlight regions where tERK in the optic tectum neuropil  
5  
6 725 fails to closely abut the cellular layer.  
7  
8 726 (e) Mean cross-correlation values for the tERK expression pattern after registration of 6 brains to  
9  
10 727 tERK<sub>ZBB</sub>, varying each of the parameters for the ANTs SyN transform, starting with the parameters that  
11 728 gave the best registration for live *vglut2a:dsRed* based registration (Syn[0.05,6,0.5]). Bottom right: MCCs  
12  
13 729 after varying the radius of the cross-correlation metric used during registration.  
14  
15 730 (f) MCCs for tERK in the same brains as in (e), after combining the two best parameter sets from (e)  
16 731 (SyN[0.1,6,0.5] and Syn[0.05,6,0]) to assess further improvement in registration precision.  
17  
18 732 (g) Horizontal section for comparison of tERK stain revealing cell morphology in the pallium after  
19 733 registration with optimal parameters for live *vglut2a* registration (left), and optimal parameters for  
20  
21 734 registering fixed and stained tissue (right).  
22  
23 735 (h,i) Same brains as in (c,d), but after registration to tERK<sub>ZBB</sub> using the parameters optimized for fixed  
24  
25 736 tissue registration.  
26  
27 737 (j,k) Horizontal section through the optic tectum showing tERK expression (red) and *vglut2a:dsRed*  
28 738 expression (green) in ZBB<sub>1,2</sub> (j) and Z-Brain (k). Matching slices within the optic tectum were selected;  
29 739 because the rotation around the y-axis is slightly different, sections are different within the medulla.  
30

31 740  
32  
33 741  
34 742

35 743 **Figure 4. Transformation between Z-Brain and ZBB coordinate systems using multi-channel**  
36  
37 744 **registration**

38 745 (a) MCC for the expression patterns of *gad1b*, *glyT2*, *isl1*, *isl2b*, *tERK*, *vglut2a* and *vmat2* and the metrics  
39  
40 746  $M_1$  and  $M_2$ , after registration of Z-Brain to ZBB<sub>1,2</sub> using either CMTK or ANTs SyN with fixed-tissue  
41  
42 747 registration parameters and the indicated combination of reference channels (*vglut2a*, *tERK<sub>REF</sub>*, *vmat2*,  
43 748 *isl2b* and *elavl3*). Note, similar results were obtained using the *tERK<sub>AV</sub>* instead of the *tERK<sub>REF</sub>* channel, but  
44  
45 749 are omitted for clarity. The combination of reference channels selected for co-registration of Z-Brain and  
46  
47 750 ZBB is highlighted.  
48  
49 751 (b) Transverse view through the caudal optic tectum showing the *vglut2a* pattern in ZBB<sub>1,2</sub>, Z-Brain, Z-  
50 752 Brain after registration to ZBB with CMTK (ZBrain-CMTK), or with ANTs (ZBrain-SyN). The torus  
51  
52 753 longitudinalis (TL) is well separated from tectal neurons in live scans, but less so in fixed tissue (arrows).  
53 754 The TL appears flattened after CMTK registration, but retains normal morphology after registration with  
54  
55 755 ANTs SyN.  
56  
57 756 (c) A comparison of transverse views as in (b), but slightly more caudal with contrast increased to  
58 757 highlight ventral distortion artifacts produced by registration (arrowheads).  
59  
60  
61  
62  
63  
64  
65

1  
2  
3  
4 758 **(d-g)** Brain Browser views in the ZBB<sub>1,2</sub> coordinate **(d,e)** or Z-Brain coordinate **(f,g)** space. Scale bars 25  
5  
6 759  $\mu\text{m}$  except 50  $\mu\text{m}$  in **(e)**  
7  
8 760 **(d)** Horizontal (top) and sagittal (bottom) slices, comparing the *Pet1:GFP* expression pattern in the  
9  
10 761 superior raphe in ZBB<sub>1,2</sub> (red) and Z-Brain after transformation to the ZBB coordinate system (green).  
11  
12 762 **(e)** Horizontal (top) and coronal (bottom) slices through the medulla oblongata, showing the expression of  
13  
14 763 *y264Et* from ZBB<sub>1,2</sub> (red) and *s1181Et* from ZBB-transformed Z-Brain (green), which both label the  
15  
16 764 Mauthner cells (arrowhead).  
17  
18 765 **(f)** Horizontal (top) and coronal (bottom) slice through the pretectum, comparing the expression of  
19  
20 766 *DAT:GFP* from ZBB<sub>1,2</sub> after transformation to Z-Brain coordinates (red) and anti-tyrosine hydroxylase  
21  
22 767 staining in Z-Brain (green).  
23  
24 768 **(g)** Horizontal (top) and coronal (bottom) slice through the medulla oblongata for *glyT2:GFP* from  
25  
26 769 ZBB<sub>1,2</sub> after transformation to Z-Brain (red) and the same transgenic line in Z-Brain (red).  
27  
28 770 **(h-k)** Brain Browser horizontal slices showing manually segmented regions transformed from the Z-Brain  
29  
30 771 coordinate system to ZBB<sub>1,2</sub> (white outlines) compared to regions previously defined in ZBB obtained by  
31  
32 772 thresholding expression patterns in transgenic lines (magenta). Regions are the torus longitudinalis **(h)**,  
33  
34 773 habenula **(i)**, anterior commissure **(j)** and trigeminal ganglion **(k)**.  
35  
36 774

### 37 775 **Figure 5. 3D visualization of brain browser data**

38 776 (a) X3D zebrafish brain shown in HTML5 Web browser and (b) Virginia Tech HyperCube (CAVE)  
39 777 (c) Virtual reality brain rendered using the Unity Game Engine for stereoscopic viewing using the Google  
40 778 cardboard viewer. (d) In the VR browser, brain regions are selected using a menu on the floor of the  
41 779 virtual arena.  
42

43 780

### 44 781 **Additional Material**

45 782

### 46 783 **Additional File 1.pdf**

### 47 784 **Point-based landmarks for manual quantification of registration precision.**

48 785 **(a)** Landmarks used for manually measuring registration precision. Position specifies the coordinates on  
49 786 *vglut2a<sub>ZBB</sub>* (transverse, horizontal, sagittal). View indicates whether the image plane shown in (b) is or  
50 787 transverse (T), horizontal (H), or sagittal (S).  
51 788 **(b)** Images of the landmarks in *vglut2a<sub>ZBB</sub>* (red) used for measuring precision.  
52 789 **(c)** Position of the landmarks superimposed on dorsal (top) and sagittal (bottom) maximum projections of  
53 790 *elavl3* through the larval brain.  
54  
55  
56  
57  
58

59 791



1  
2  
3  
4  
5  
6  
7  
8  
9  
10  
11  
12  
13  
14  
15  
16  
17  
18  
19  
20  
21  
22  
23  
24  
25  
26  
27  
28  
29  
30  
31  
32  
33  
34  
35  
36  
37  
38  
39  
40  
41  
42  
43  
44  
45  
46  
47  
48  
49  
50  
51  
52  
53  
54  
55  
56  
57  
58  
59  
60  
61  
62  
63  
64  
65

792 **Additional File 2.doc**

793 **Instructions for using transformation matrices to convert between ZBB and Z-Brain coordinate**  
794 **systems.**

795

Method	Step	Function	Command
Live Registration	1	Register vglut2a pattern in fish1-01.nii.gz, to the reference brain ref/vglut-ref.nii	antsRegistration -d 3 --float 1 -o [fish1_fish1_Warped.nii.gz] --interpolation WelchWindowedSinc --use-histogram-matching 0 -r [ref/vglut-ref.nii,fish1-01.nii.gz,1] -t rigid[0.1] -m MI[ref/vglut-ref.nii,fish1-01.nii.gz,1,32,Regular,0.25] -c [200x200x200x0,1e-8,10] --shrink-factors 12x8x4x2 --smoothing-sigmas 4x3x2x1vox -t Affine[0.1] -m MI[ref/vglut-ref.nii,fish1-01.nii.gz,1,32,Regular,0.25] -c [200x200x200x0,1e-8,10] --shrink-factors 12x8x4x2 --smoothing-sigmas 4x3x2x1vox -t SyN[0.05,6,0.5] -m CC[ref/vglut-ref.nii,fish1-01.nii.gz,1,2] -c [200x200x200x10,1e-7,10] --shrink-factors 12x8x4x2x1 --smoothing-sigmas 4x3x2x1x0vox
	2	Apply transformation matrix from (1) to a second channel for fish 1, in file fish1-02.nii.gz	antsApplyTransforms -d 3 -v 0 --float -n WelchWindowedSinc -i fish1-02.nii.gz -r ref/vglut-ref.nii -o fish1-02_Warped.nii -t fish1_1Warp.nii.gz -t fish1_0GenericAffine.mat
Fixed registration	1	Register tERK pattern in fish1-01.nii.gz, to the reference brain ref/terk-ref.nii	antsRegistration -d 3 --float 1 -o [fish1_fish1_Warped.nii.gz] --interpolation WelchWindowedSinc --use-histogram-matching 0 -r [ref/terk-ref.nii,fish1-01.nii.gz,1] -t rigid[0.1] -m MI[ref/terk-ref.nii,fish1-01.nii.gz,1,32,Regular,0.25] -c [200x200x200x0,1e-8,10] --shrink-factors 12x8x4x2 --smoothing-sigmas 4x3x2x1vox -t Affine[0.1] -m MI[ref/terk-ref.nii,fish1-01.nii.gz,1,32,Regular,0.25] -c [200x200x200x0,1e-8,10] --shrink-factors 12x8x4x2 --smoothing-sigmas 4x3x2x1vox -t SyN[0.1,6,0] -m CC[ref/terk-ref.nii,fish1-01.nii.gz,1,2] -c [200x200x200x10,1e-7,10] --shrink-factors 12x8x4x2x1 --smoothing-sigmas 4x3x2x1x0vox
	2	Apply transformation matrix from (1) to a second channel for fish 1, in file fish1-02.nii.gz	antsApplyTransforms -d 3 -v 0 --float -n WelchWindowedSinc -i fish1-02.nii.gz -r ref/terk-ref.nii -o fish1-02_Warped.nii -t fish1_1Warp.nii.gz -t fish1_0GenericAffine.mat

Table 1

No.	Landmark	CMTK	ANTs/mcc	ANTs/visual	ref. brain
1	Middle of left nerve from olfactory epith to brain	6.5	6.6	8.2	5.8
2	Anterior-most extension of left-habenula	4.2	2.7	3.6	3.0
3	Ventral-most part of right-preoptic area cell cluster	8.0	5.0	6.3	4.2
4	Middle of neuropil zone of tectum griseum (right)	5.0	4.6	8.0	4.0
5	Dorsal exit point of nerve from left torus semicircularis	2.9	2.8	5.0	2.8
6	Mid-point of projections to caudal hypothalamus	7.8	10.6	5.2	3.6
7	Right medial tip of cerebellum caudal lobe tip	4.2	1.8	3.4	3.5
8	Middle of R5 commissure	1.9	1.4	3.5	1.8
9	Ventral-most cluster of cells in medial/caudal medulla	15.2	7.4	11.9	11.8
10	Dorsal/anterior-most point of midline cell group in ventral/caudal medulla	5.8	8.4	7.1	4.9
Mean distance from landmark in reference brain (microns)		6.1 ± 1.2	5.1 ± 1.0	6.2 ± 0.90	4.5 ± 0.9

**Table 2**

ZBB			zBrain		Registration channel?	Quantification metric?
<i>Tg(vGlut2a:DsRed)nns14</i>	mean of 346 brains	↔	<i>Tg(vGlut2a:EGFP)zf139</i>	mean of 15 brains	y	y
<i>Tg(vGlut2a:DsRed)nns14</i>	single reference brain	↔	<i>Tg(vGlut2a:EGFP)zf139</i>	mean of 15 brains	y	n
<i>Tg(elavl3:CaMPARI)jf9</i>	mean of 3 brains	↔	<i>Tg(elavl3:GCaMP5G)a4598</i>	mean of 7 brains	y	n
<i>Tg(vmat2:GFP)pk2</i>	mean of 3 brains	↔	<i>Tg(vmat2:GFP)pk2</i>	mean of 55 brains	y	y
<i>Tg(isl2b:GFP)zc7</i>	mean of 3 brains	↔	<i>Tg(isl2b:GFP)zc7</i>	mean of 8 brains	y	y
<i>tERK immunostain</i>	mean of 167 brains	↔	<i>tERK immunostain</i>	mean of 197 brains	y	y
<i>tERK immunostain</i>	single brain	↔	<i>tERK immunostain</i>	single reference brain	y	n
<i>Tg(isl1:GFP)rw0</i>	mean of 3 brains	↔	<i>Tg(isl1:GFP)rw0</i>	mean of 17 brains	n	y
<i>TgBAC(gad1b:GFP)nns25</i>	mean of 4 brains	↔	<i>TgBAC(gad1b:GFP)nns25</i>	mean of 10 brains	n	y
<i>Tg(glyT2:GFP)cf3</i>	mean of 6 brains	↔	<i>Tg(glyT2:GFP)cf3</i>	mean of 13 brains	n	y

Table 3

No.	Landmark	CMTK/tERK	CMTK/vglut	ANTS
1	Middle of left nerve from olfactory epith to brain	26.0	8.8	9.6
2	Anterior-most extension of left-habenula	11.7	7.3	5.7
3	Ventral-most part of right-preoptic area cell cluster	32.1	37.8	7.0
4	Middle of neuropil zone of tectum griseum (right)	9.3	8.5	8.5
5	Dorsal exit point of nerve from left torus semicircularis	19.8	24.6	6.7
6	Mid-point of projections to caudal hypothalamus	34.9	44.9	11.9
7	Right medial tip of cerebellum caudal lobe tip	30.1	10.5	12.5
8	Middle of R5 commissure	9.3	5.5	2.8
9	Ventral-most cluster of cells in medial/caudal medulla	17.1	9.8	12.9
10	Dorsal/anterior-most point of midline cell group in ventral/caudal medulla	56.0	21.5	21.6
Mean distance from landmark in reference brain (microns)		24.6 ± 4.6	17.9 ± 4.4	9.9 ± 1.7

**Table 4**

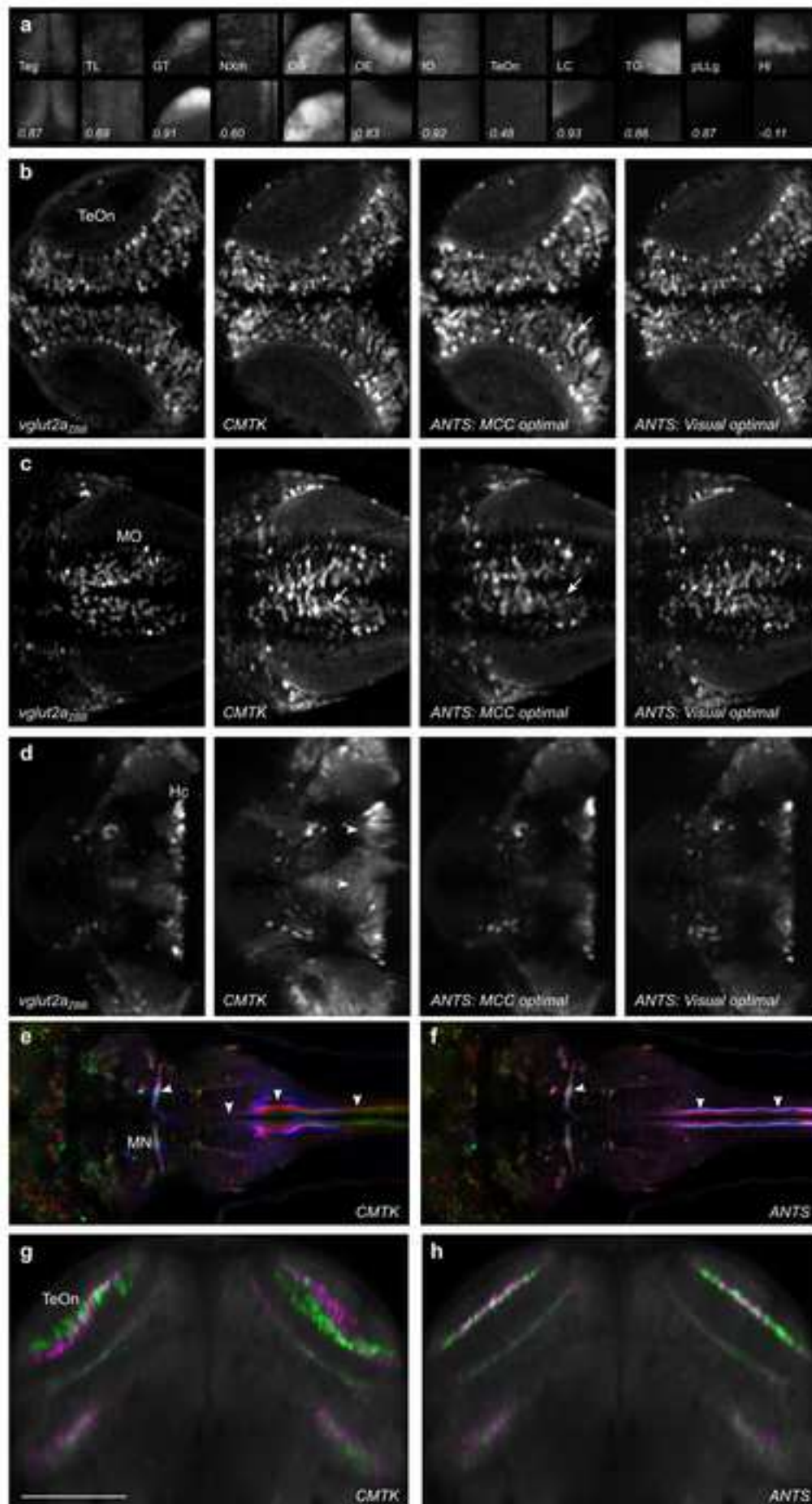


Figure 1

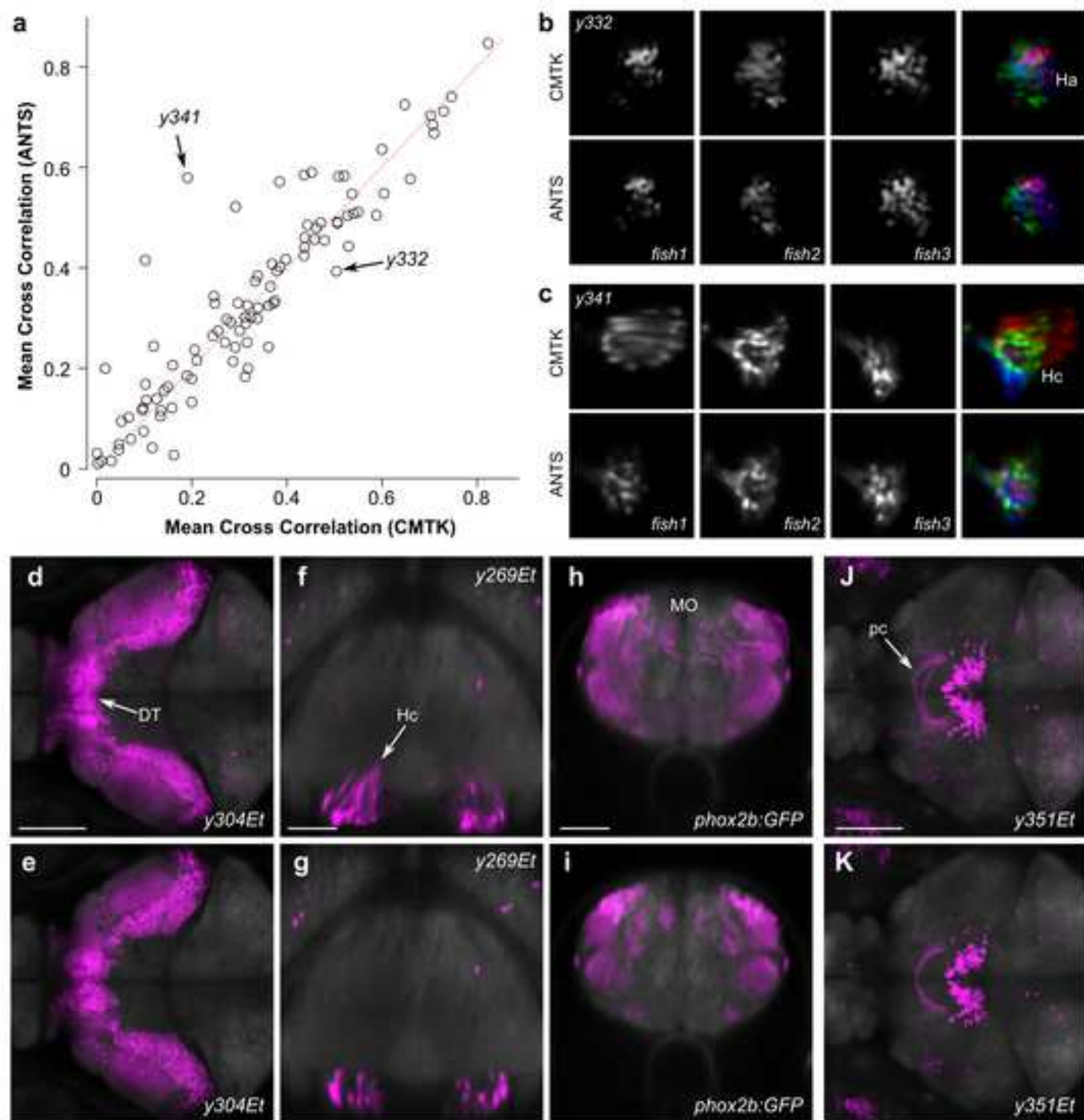


Figure 2

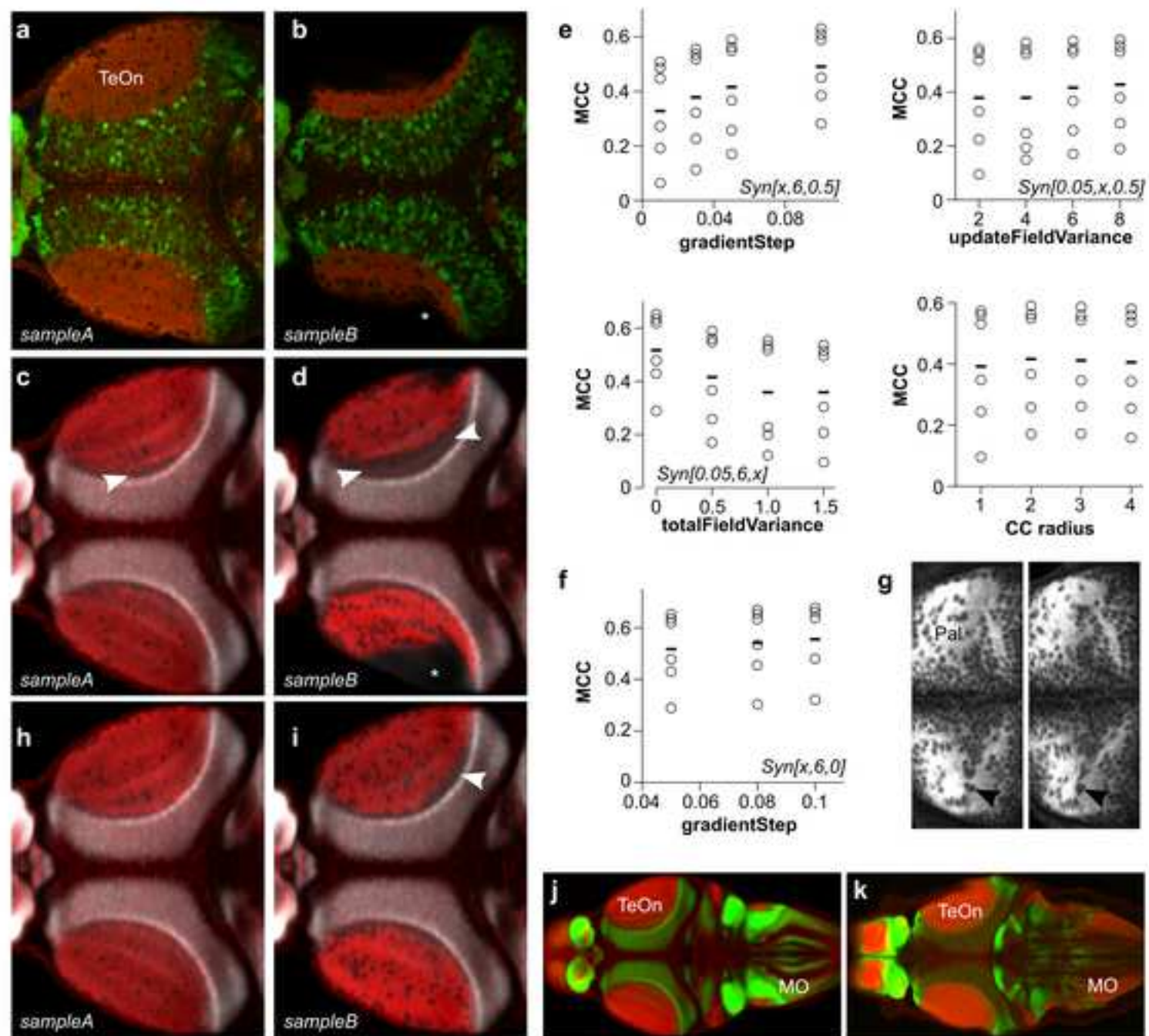


Figure 3



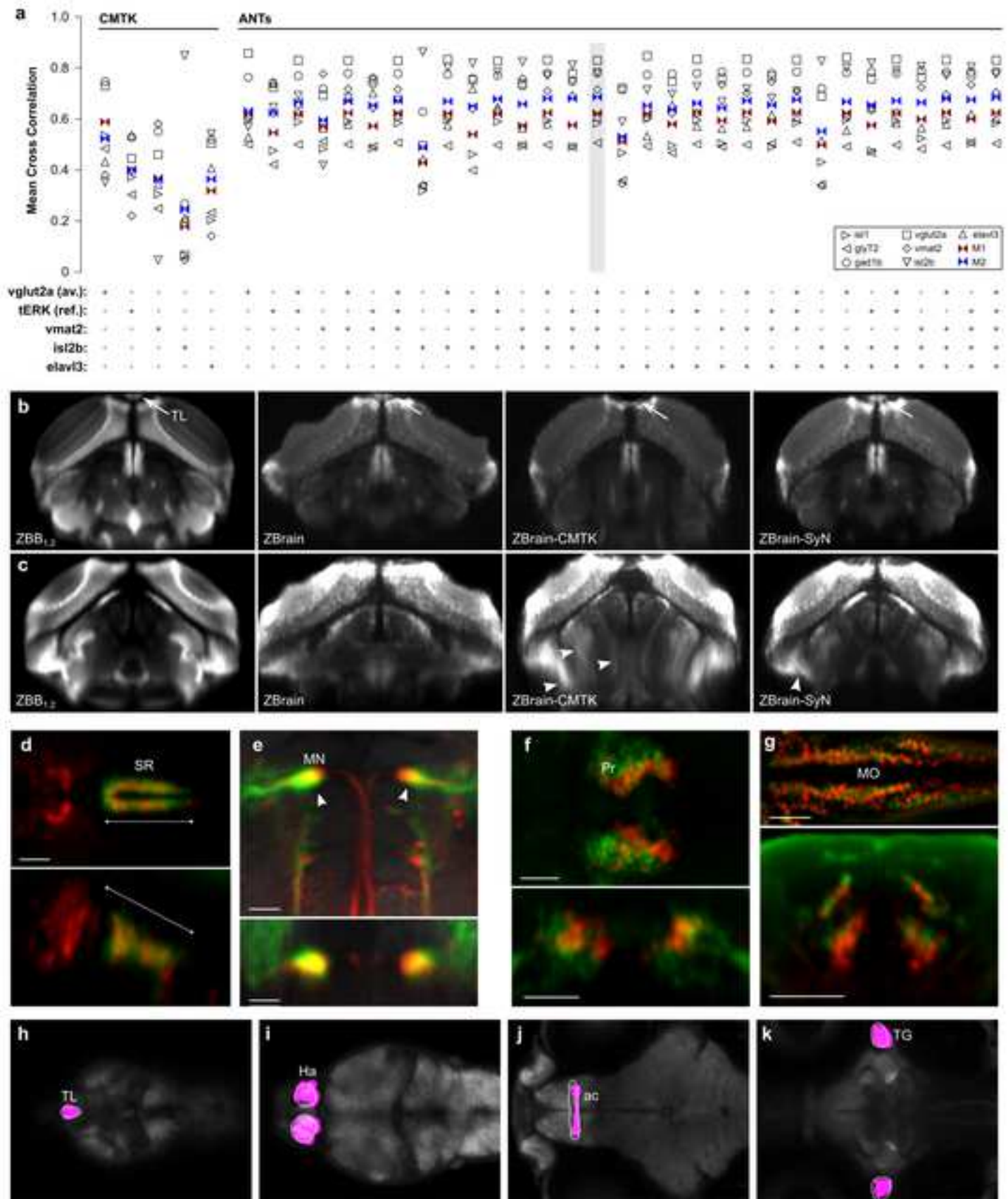


Figure 4

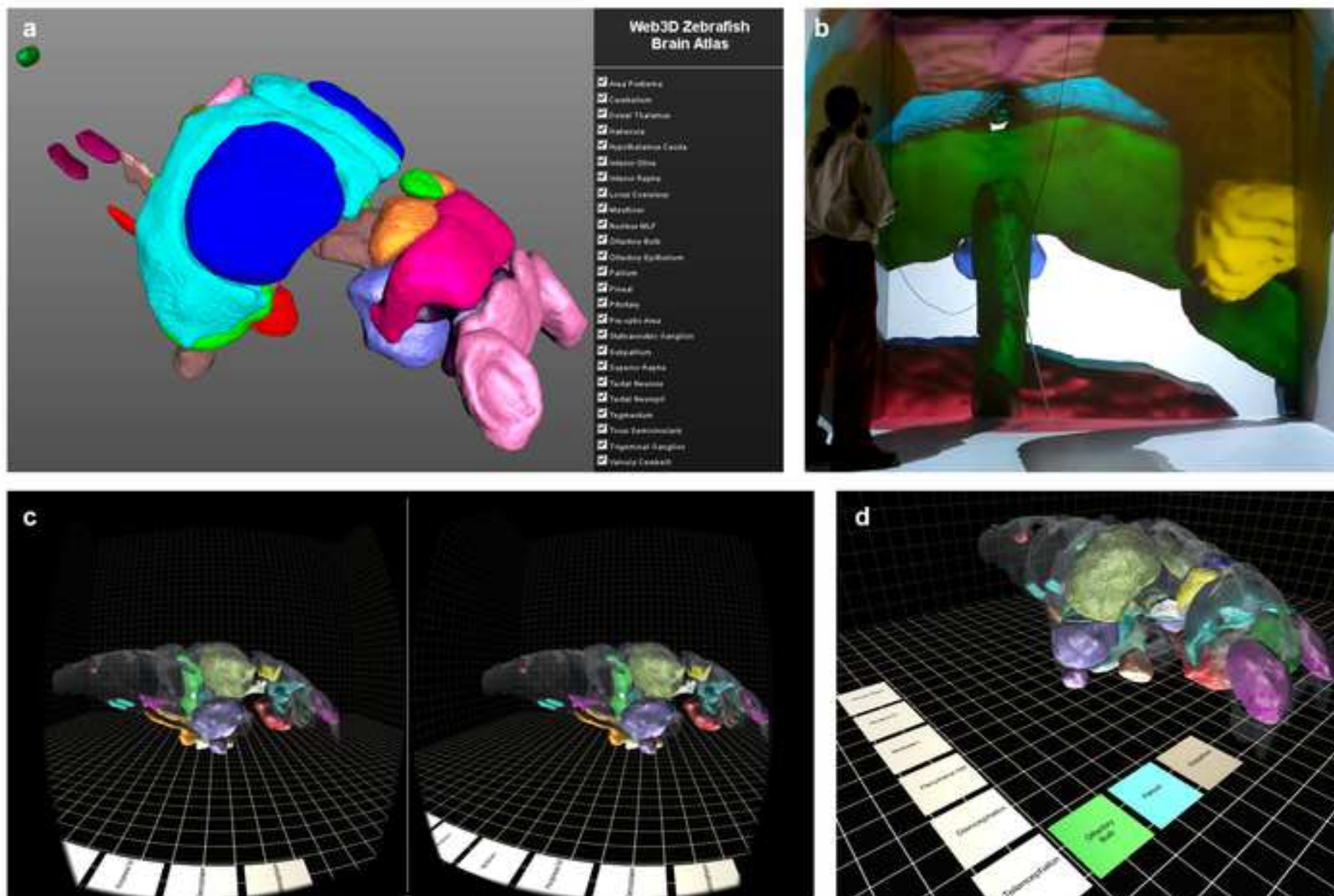

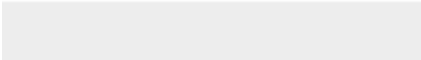

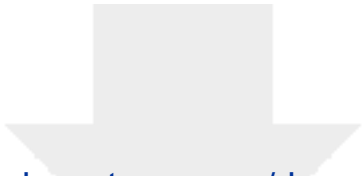


Figure 5



Click here to access/download  
**Supplementary Material**  
Additional File 1.tif





Click here to access/download  
**Supplementary Material**  
Additional File 2.docx

